Phase-averaged characterization of turbulent isothermal free swirling jet after vortex breakdown

R. Sharma[1,*], F. Cozzi[1], A. Coghe[1]
1: Department of Energy, Politecnico di Milano, Milano, Italy
* Correspondent author: rohit.sharma@polimi.it

Keywords: 3C-2D PIV, Swirling flow, vortex breakdown, PVC, POD

ABSTRACT

This work mainly focused on the near-exit region of a round isothermal free swirling jet to characterize the effect of swirl on the flow field and to identify large coherent structures. 3C-2D PIV was employed to capture the instantaneous flow field close to the nozzle exit for non-swirling (S=0) and a high swirling jets (S=1.26) both with a Reynolds number of 21800. At swirl level of 1.26 the pressure fluctuations measured by a capacitive microphone indicate the existence of periodic instability, the so called precessing vortex core (PVC). A three-component proper orthogonal decomposition (POD) applied to the instantaneous velocity fields allow to identify the dominant flow structure associated to the PVC. The time coefficients of the two first most energetic POD modes were used to reconstruct the phase of the oscillatory motion in the swirling flow. The phase information was then used to conditionally average the instantaneous velocity fields, this allowed the 3D structure of the PVC to be reconstructed. The instantaneous minima of negative swirling strength values calculated from the instantaneous velocity field revealed the presence of two helical structures located in the inner and outer shear layers. By phase averaging the instantaneous swirling strength maps, the 3D helical vortex structure was reconstructed. The two co-winding counter-rotating helical structure fade out at an axial location of approximately z/ D = 1.5. The findings evidence that the combined application of PIV, POD and frequency analysis using capacitive microphone can provide detailed observations of coherent fluctuations induced by vortex precession.

1. Introduction

Swirling flows are commonly find in most practical applications such as gas turbine combustors, swirl burner, furnaces, spraying machine, whirlpools, cyclone separators and vortex shedding from aircraft wings (Gupta et al. 1984). The swirl intensity effects in flow fields are well described in the literature (e.g Gupta et al. (1984), Billant et al. (1998), Panda et al. (1993)). When the degree of swirl above a critical value (i.e. S_{cr} = 0.6), vortex breakdown occurs bringing to a significant change in the flow structure (Gupta et al. (1984)). Various form of breakdown has been identified and different mechanisms for its onset have been proposed (Lucca-Negro and O'Doherty (2001)). Another well-known instability is relevant to swirling flows, the so called PVC which is periodic in nature and it is usually associated with the vortex breakdown and the

existence of a central recirculation zone. Jet precession is also known to occur even in low swirling jets [Chanaud et al. (1965)]. Despite the related number of experimental, theoretical and numerical studies the vortex breakdown and the PVC phenomena are still not fully understood [Lucca-Negro et al. (2001), Syred et al. (2006), Martinelli et al. (2012)].

In recent year, experimental techniques such as PIV or LDV associated with data treatment able to extract the coherent structure embedded in the flow or either the amplitude of the periodic velocity fluctuations have grown in popularity and have been applied to many different complex flow, for e.g flow in cylinder wakes ((Negri et al. (2010) & Oudheusden et al (2005)), swirling flow ((Oberleithner et al. (2011), Stohr et al. (2011)) and in-cylinder engine flows (Chen et al. (2012) just to cite a few. Proper orthogonal decomposition (POD) technique is one of the data analysis tools often used to extract coherent structure in PIV measurements. Lumley et al. (1967) is generally attributed as being the first to suggest POD application to analyze coherent structure in turbulent flows. In the case of periodic oscillation, a special feature of POD is its ability to determine the phase with respect to the periodic cycle proposed by Oudheusden et al. (2005). Oudheusden et al. investigated the vortex shedding combining non-time resolved PIV measurements and POD analysis. They used the first two POD coefficients as the global phase indicator, the latter was then used to phase average the velocity maps. Stohr et al. (2011) used the same technique to investigate the flame-vortex interaction. They found that the small scale structures are represented more accurately in the phase averages as compared to the low order model. In a similar way Oberleithner et al. (2011) applied POD analysis to phase average non-time resolved PIV snapshots of a precessing swirling jet, the 3D periodic structure was reconstructed from the phase averaged PIV maps. Oberleithner et al. claimed that being based on spatial modes a more accurate prediction of the phase angle can be get from POD as compared to using single point time resolved measurement, unless too few samples are used in the phase average.

The objective of the present experiments is to investigate the 3D helical vortex structure emerging in the unconfined free swirling turbulent jet associated with the vortex breakdown and PVC through the combination of Stereo-PIV measurements and POD analysis. A detailed analysis of the influence of swirl intensity on central recirculation zone, vortex breakdown, and precession frequencies has been reported in a previous work, see Cozzi et al. (2015). Proper orthogonal decomposition is applied in both longitudinal and transverse plane PIV data to characterize the effect of the influence of swirling intensity on the structure of swirling jet. The POD correlation coefficients of the first two most energetic modes were used for phase

identification and thereby to phase average the instantaneous flow field. The phase averaged velocity maps were then used to reconstruct the organized vortical structures.

2. Experimental set up and data processing technique

2.1. Experimental apparatus

A vertically mounted swirl generator was used to generate isothermal free swirling air jets as shown in Figure 1. The swirl generator consists of a pipe of 80 mm in diameter and about 180 mm in length, it is followed by a converging section of 160 mm length, at the end of the converging section is located a cylindrical nozzle of 40 mm in length and internal diameter D=36 mm. The swirl generator is of axial-plus-tangential entry type, it allows changing swirl intensity by varying the axial and tangential flow rates of air by means of thermal mass flow meters with 1% accuracy. The axial air enters through four radial inlets in the cylindrical chamber and passes through a plate with 24 numbers of holes of 2 mm in diameter to produce a uniform axial stream. The tangential air is introduced through eight tangential inlets to impart angular momentum, upstream from the burner throat.

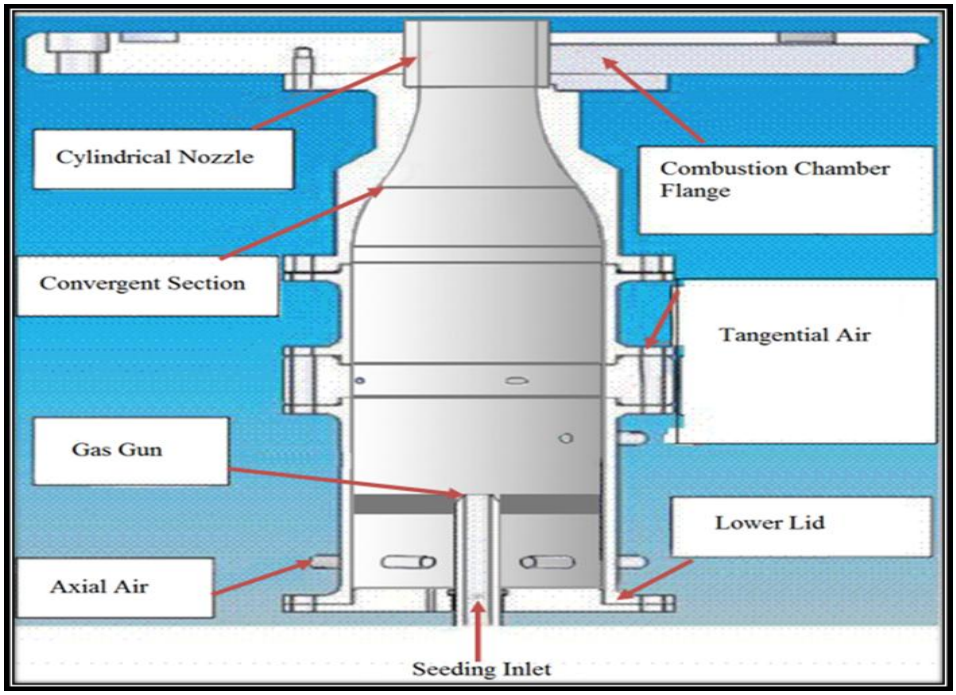

Fig. 1 Experimental set-up of swirling burner

2.2. *Measurement techniques*

3C-2D Stereoscopic PIV was employed to characterize the flow field patterns under isothermal conditions. The velocity field of the swirling jet was measured at the nozzle exit in a vertical plane. A double pulse Nd:YAG laser (energy ≈ 200 mJ/ pulse; λ = 532 nm) unit enabled to measure velocity vectors in the axial-radial direction. Here, a laser sheet (approximate thickness of about 1-1.5mm) fired vertically close to the exhaust of the burner illuminated fine particles of oil droplets. Two CCD cameras of 1344 * 1024 pixels each equipped with a Nikon lens of 60 mm focal length were mounted according to the Scheimpflug rules, they view the laser sheet from opposite side at about the same angle of 45° and both the cameras were oriented in the particle's forward scattering direction. Measurements were conducted in double frame mode with time between pulses of the order of 10-30 μs, depending on the swirl intensity and double images were acquired at a rate of 5 Hz. The jet flow was seeded with oil droplets with average diameter of 1-2 μm produced by a jet atomizer; the seeding is injected inside the swirl generator through a central pipe (gas gun), to avoid interference with the swirling flow the gas gun exit is located about 8D below the exit plane of the nozzle. The external seeding particles are homogeneously distributed throughout the measurement plane and generated by a six-jet Atomizer. Dantec's DynamicStudio software is used to acquire and to process the images. The raw images were subjected to an image balancing filter with a smooth cell size of 5 x 5 to correct the non-uniformities of laser light sheet prior to cross-correlation. An adaptive cross correlation algorithm, including peak validation and 50% overlap area is implemented. The final size of the interrogation area is 32x32 pixels. Finally the third velocity component is reconstructed from the two 2D vectors fields by using the method proposed by Soloff et al. (1997) and implemented in the Dantec software. Average flow map were obtained by averaging 700 instantaneous vector fields.

Two different configuration were used: in the first one the laser sheet was fired perpendicular to the jet axis and about 3 mm above the nozzle exit (transverse plane), in the second one the laser sheet passed through the vertical axis of the burner (meridional or longitudinal plane) as shown in Figure 2(a&b). Thus the out of plane velocity components in the first and in second case respectively were the axial velocity and the azimuthal velocity. For the transverse plane the resolution in the 3C velocity maps was about 1.1 × 1.2 mm^2, while for the meridional plane the resolution was about 2.5 × 1.7 mm^2.

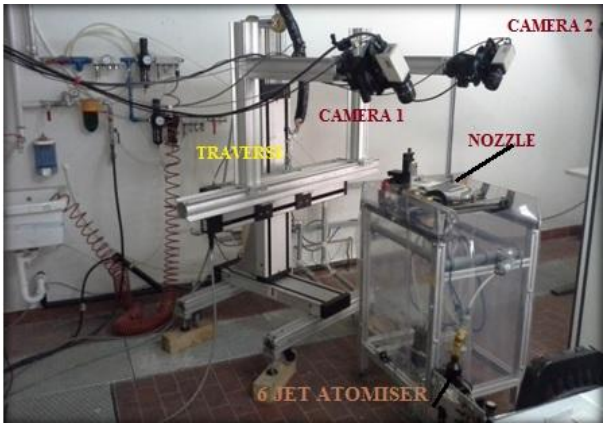

(a)

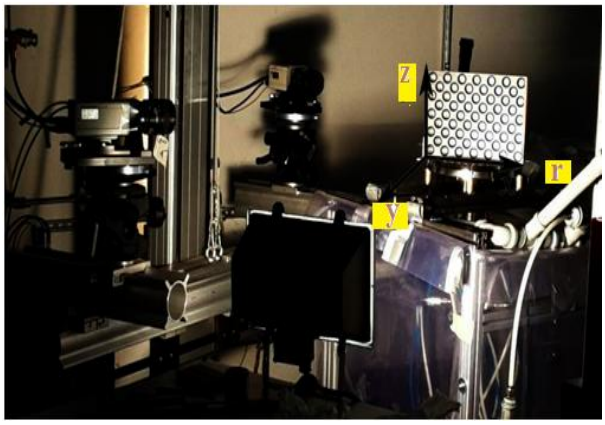

(b)

Fig. 2 Experimental set-up: **(a)** camera oriented for transverse plane measurements and **(b)** for longitudinal plane measurements.

3. Methodology and characterization parameters

The swirl intensity for rotating flows is usually characterized by the non-dimensional swirl number, given by

$$S = \frac{G_\theta}{G_z R} \qquad (1)$$

which represents the ratio of the axial flux of angular momentum, G_θ, to the axial flux of axial momentum, G_z, times a nozzle radius, R, Chigier and Chervinsky (1967). Swirl number can be written in number of ways depending on the assumptions (Gupta et al. (1984), Chigier and Chervinsky (1967)), by neglecting contribution from turbulent component and expressing the one due to pressure in terms of azimuthal velocity (see Rajaratnam et al. (1976)). Equation.1 can be rewritten as

$$S_1 = \frac{2\pi\rho \int_{-r}^{r} r^2 UW dr}{2\pi\rho \left[\int_{-r}^{-r} r(U^2 - \frac{1}{2}W^2) dr\right] \times R} \qquad (2)$$

The definition of swirl number S1 is used here to characterize the flow field where U, W and ρ are the time averaged axial velocity, time mean azimuthal velocity, and air density respectively. The swirl number is evaluated at the same downstream position for both transverse and longitudinal plane with the integration limit on radial distance (r) by applying threshold on axial velocity; limits were set at ≤0.1 m/ s.

With axial plus tangential swirl generator it was found by Claypole and Syred (1981) that a convenient way to examine the swirl number was to use the axial and tangential mass flow rates to determine a geometric swirl number (S_g) which is given by

$$S_g = \frac{\pi R_o R}{A_T}\left(\frac{\dot{m}_{tangential}}{\dot{m}_{tangential}+\dot{m}_{axial}}\right)^2 \qquad (3)$$

where R_o = radial distance of tangential inlets from burner axis, R = nozzle radius, A_T = total area of tangential air inlets, $\dot{m}_{tangential}$ and $\dot{m}_{axial}$ = mass flow rate of tangential and axial air inlets. Swirl numbers calculated using Equations 2 and 3 are shown in Table A. Swirl number (S = 1.26) is taken as reference for comparison in both transverse and longitudinal plane.

The Reynolds number Re = (ρ*Umean*D)/ μ is based on nozzle diameter, D=2R, the bulk mean velocity, Umean, and the dynamic air viscosity, μ. The acquired 700 instantaneous velocity fields were averaged to calculate the mean flow field and in addition, the POD method was employed to decompose the velocity field into energy containing modes, calculate eigen values and therefore analyze the flow structure and instabilities in more detail.

Table A. Experimental Conditions

Reynold's number = 21800	**S_g**	**S_1**
Transverse plane (z/ D = 0.08)	0	0
	4.6	1.4
Longitudinal plane	0	0
	4.6	1.26

4. Proper Orthogonal Decomposition

The POD method decomposes the original instantaneous velocity field into modes and their corresponding energies (or eigenvalues). It is obvious to apply the POD to velocity, since the optimization of the basis in L^2 space separates and ordering the mode according to the energy which usually associated with the large scale flow structures (Berkooz et al (1993)). The method of snapshots (Sirovich et al. (1987)) which is known to be computationally efficient it is used

here. Here each instantaneous velocity measurement by PIV is considered to be a snapshot of the flow. An analysis is then performed on the 700 snapshots acquired in both transverse and longitudinal plane under identical experimental conditions. The first step is to calculate the mean velocity field. The mean velocity field can be considered as the zeroth mode of the POD. The principal idea behind POD is to calculate a set of linear basis functions, also called POD modes, which represents the fluctuating parts of the velocity components of the flow (u_j^n, v_j^n, w_j^n) where u, v, w represents the fluctuating parts of each of the three velocity components. Index n runs through the N snapshots and j runs through the M positions of velocity vectors in a given snapshots i.e. $u_j = u(x_j, y_j, z_j)$. All fluctuating velocity components from the N snapshots arranged in a matrix U as:

$$U = [u^1 \quad u^2 \quad \cdots \quad u^N] = \begin{bmatrix} u_1^1 & u_1^2 & \cdots & u_1^N \\ \vdots & \vdots & \vdots & \vdots \\ u_M^1 & u_M^2 & \cdots & u_M^N \\ v_1^1 & v_1^2 & \vdots & v_1^N \\ \vdots & \vdots & \cdots & \vdots \\ v_M^1 & v_M^2 & \vdots & v_M^N \\ w_1^1 & w_1^2 & \cdots & w_1^N \\ \vdots & \vdots & \vdots & \vdots \\ w_M^1 & w_M^2 & \cdots & w_M^N \end{bmatrix} \qquad (4)$$

The NxN autocovariance matrix C is created from the U matrix as:

$$C = U^T U \qquad (5)$$

and the corresponding eigenvalue is calculated as

$$CB_i = \lambda_i B_i \qquad (6)$$

where λ_i and B_i are corresponding eigenmodes and eigenvectors. The modes are arranged such that their energies are sorted according to the size of their eigenvalues:

$$\lambda_1 > \lambda_2 > \lambda_3 > \ldots\ldots\ldots\ldots \lambda_N = 0 \qquad (7)$$

According to such sorting criteria, the periodic motion in complex flow is always represented by the first several modes. The eigenvectors corresponding to each of the eigenvalues make up a basis for constructing the eigen-functions, which are normalized to get POD modes Φ_i:

$$\phi_i = \frac{UB_i}{|UB_i|}, i=1,2,.....N-1 \qquad (8)$$

where B_i is the ith eigenvector corresponding to the eigenvalue λi and modes are normalized by discrete 2-norm defined as :-

$$\|y\| = \sqrt{y_1^2 + y_2^2 + \cdots ... y_m^2} \qquad (9)$$

Each snapshot can be expanded in a series of the POD modes, thus the velocity part of a snapshots n is representated as Eq. (10):

$$u_n = \sum_{i=1}^{N} a_i^n \phi_i^n = \varphi a^n \qquad (10)$$

POD coefficients ai for each mode i are determined by projecting the fluctuating part of the velocity field onto the POD modes:

$$a_n = \varphi^T u_n \qquad (11)$$

where $\varphi = (\phi_j^n, \phi_j^n, \phi_j^n)$.

The amount of total energy from velocity fluctuations associated with a given POD mode is proportional to the corresponding eigen value.

5. Results and discussion

5.1 Mean flow morphology

Figure 3 shown the contour plots of mean axial velocity in both transverse plane at z/ D = 0.08 and longitudinal plane for non- swirling flow (S = 0) and high swirling flow (S=1.26) and Reynolds number = 21800. For the non swirling case is shown in Figure 3(a&c), the average axial velocity resulted to be 9.45 m/ s. The jet show an almost uniform axial velocity across the jet section and a thin shear layer located on the jet border. The normalized characteristics radius, x/ D of the jet, which is defined as the distance between the jet center and the external jet position where the axial velocity is 0 ± 0.1 m / s is 0.65. The flow structure is symmetric about the central axis and enlarges in size as the flow moves downstream as shown in Figure 3(c). For high swirling flow significant changes occurs in the jet structure as compared to the non-swirling flow. The radius of the jet is expanded in the outward direction and the jet boundary moves from r/ D=0.65 to r/ D=0.78. Furthermore, the maximum axial velocity is increased to 13.85 m/ s, and at the center (vortex core) axial velocity reach a minimum value of -0.55 m/ s. This is 106 %

down compared to the core velocity of the non-swirling flow, and the 45 % rise occurs for the peak.

.

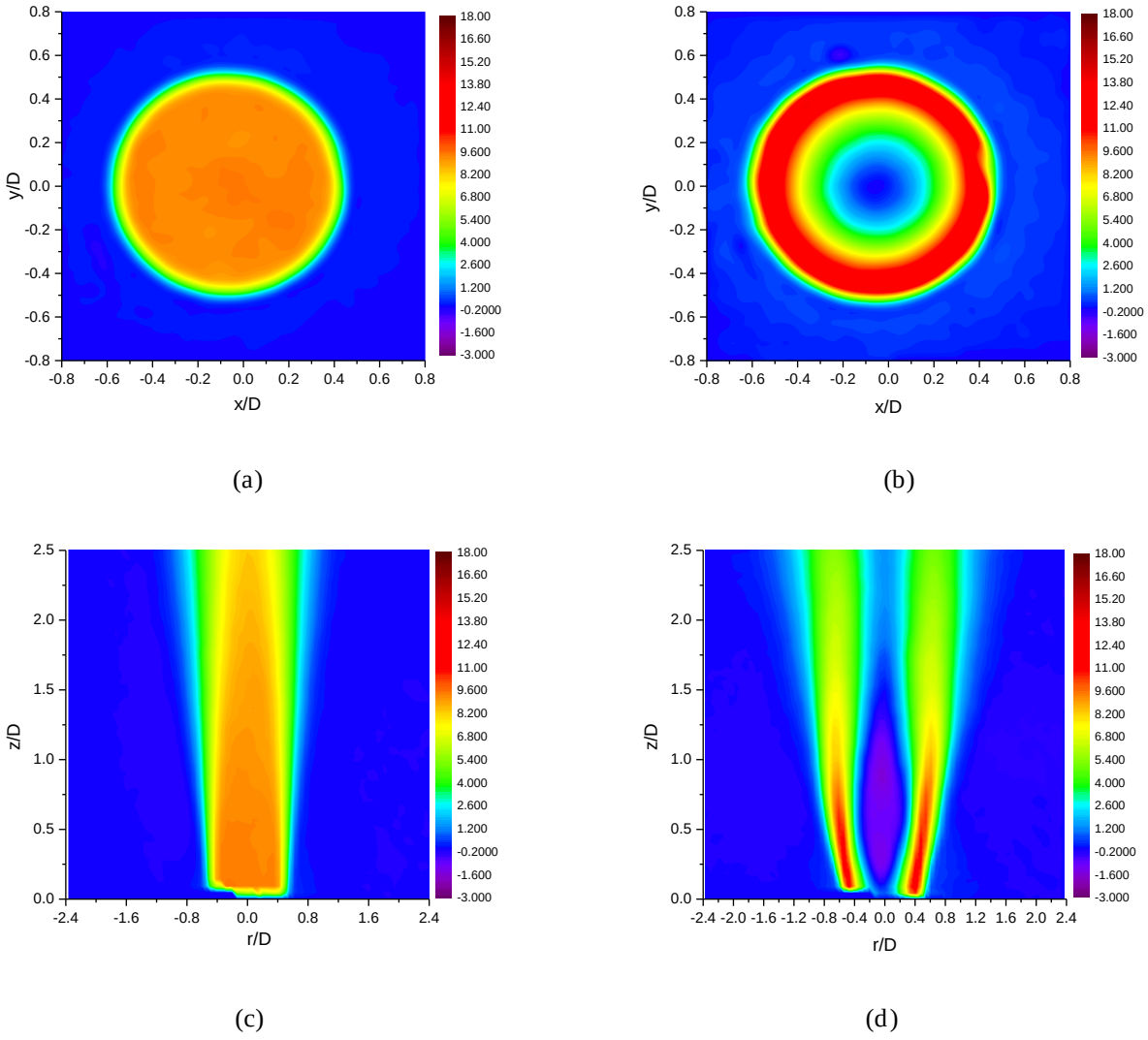

Fig. 3 Contour plots of the mean axial velocity, U in m/ s for S = 0 (left) & 1.26 (right): **(a & b)** transverse plane (z/ D = 0.08), **(c & d)** longitudinal plane.

Figure 4 (non-swirling flow, S = 0) & 5 (high swirling flow, S = 1.26), presents the radial distribution of time averaged radial, axial and tangential velocity profile and its fluctuating velocity components, normalized by the mean axial velocity. Data are presented for lowest upstream position z/ D = 0.116 and highest downstream position z/ D = 2.45.

For the non-swirling flow, the radial velocity along positive and negative r-traverse stays at almost zero except in the region of r/ D = 0.5-0.55 of both sides. The radial profile of axial velocity shows a top hat shape as shown in Figure 4a. The strong velocity fluctuations appeared

in jet core region that extended in the radial direction as the flow moves downstrean, compare Figure. 4b and 4d. The radial profile of axial velocity shows a top hat shape as shown in Figure 4a. Moving downstream and after about z/ D = 0.84 the profiles evolves to a gaussian shape and the potential core of the jet is visible up to the highest axial coordinate as shown in Figure 3c. The distribution of root mean square (rms) components of axial velocity near to the nozzle exit is shown in Figure 4b and 4d. High levels of turbulence are found in the outer shear layer and in the jet core region. The maximum fluctuations of the axial component in the shear layer region for non-swirling jet increases towards downstream and decreases in the vortex core region towards downstream approaching a bow shape profile as shown in Figure 4d.

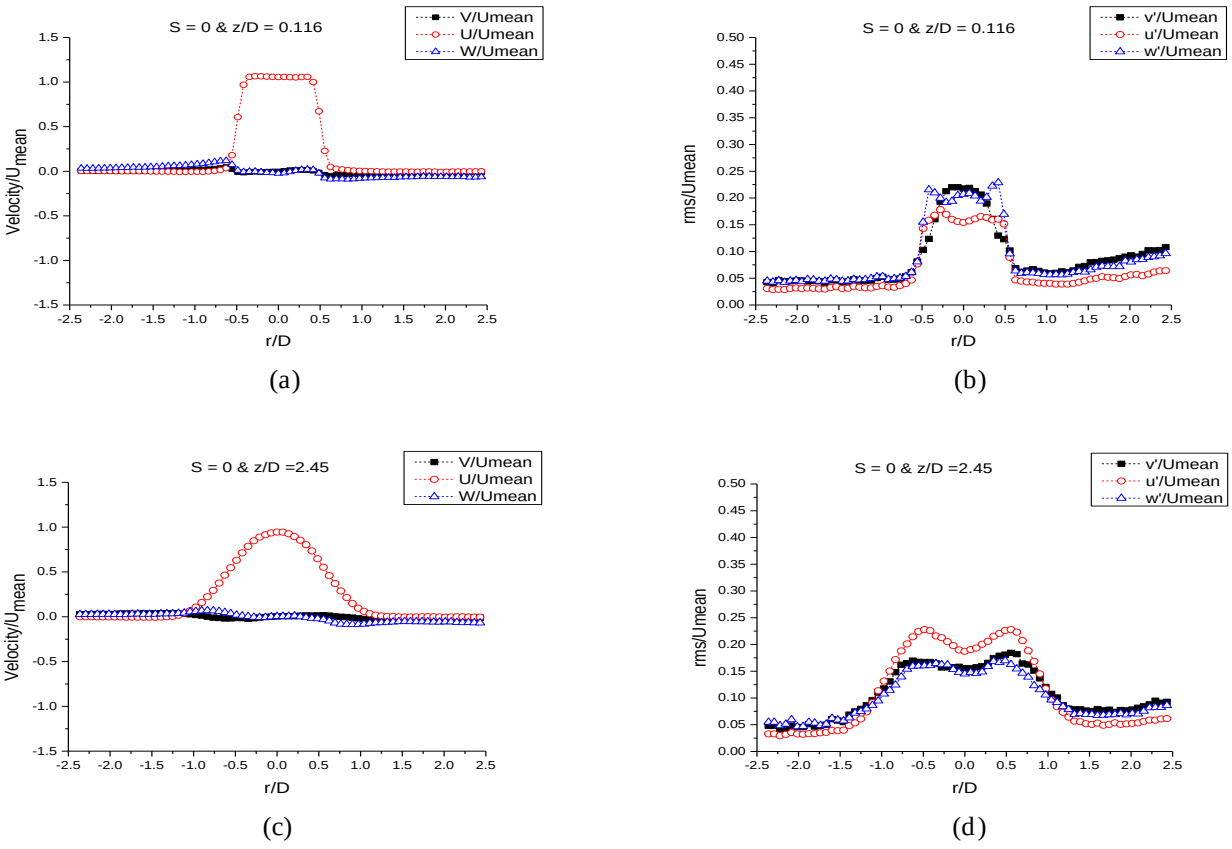

Fig. 4 (a,c) Mean (left) and **(b,d)** r.m.s (right) velocity profiles for radial (black squares), axial (red dots), tangential (blue traingles) under non-swirling conditions for Re = 21800

For swirling flow, the radial velocity increases as swirl intensity increases and after the occurrence of vortex breakdown, the magnitude of the radial velocity is somewhat comparable with the other two components. The tangential velocity induces a radial pressure gradient at the exit of nozzle which leads to raise the magnitude of radial velocity component inside the jet. The radial velocity at r/d > 0.6 is negative

in both +r and –r axis, which signifies that the atmospheric air is entrained into the jet. At the nozzle exit, regions of high velocity fluctuations are located in the inner shear layers, the outer shear layers and the vortex core region, see Figure 5b. The mean tangential velocity is antisymmetric with respect to the vertical axis of the jet shown in Figure 5a. Strong radial velocity fluctuations appear in the outer shear layer, while strong tangential velocity fluctuations occur in the inner shear layer. On the jet axis both radial and tangential velocity fluctuations show a maximum, while strongest axial velocity fluctuation occur in the inner shear layer, Figure 5b. The tangential velocity reaches the maximum at r/D = 0.5 before reaching to zero toward the jet edge. It continue to decay downstream with transfer of angular momentum to the external flow and smoothening the profile from r/D = 1.68. This change in profiles induces complex axial velocity profiles and reverse flow zone patterns as shown in axial velocity profiles, Figure 5(a&c). Near to the nozzle exit, higher level of turbulence is found in the outer shear layer and vortex core region as compared to the annular region between them. However turbulent fluctuations associated with the tangential velocity component are somewhat lower as compared to axial velocity component. The turbulence intensity in the vortex core region is higher due to recirculation zone and wobbliness produced by vortex breakdown. For strong swirl intensity vortex breakdown appeared on the jet axis. A reverse region with negative axial velocity was found downstream at z/D = 0.116. The axial velocity fluctuation distribution had maximum turbulence level in the shear layer and minimum turbulence level in the vortex core region. The magnitude of turbulence intensity increased and high turbulence region enlarged as swirl intensity increased, the velocity fluctuation distribution far away from the nozzle and in the downstream direction were almost flat with high turbulence intensity magnitude while the turbulence level in the shear layer and vortex core region was comparable, Figure 5d

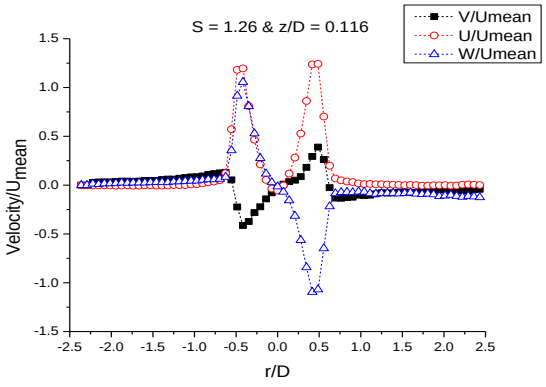

(a)

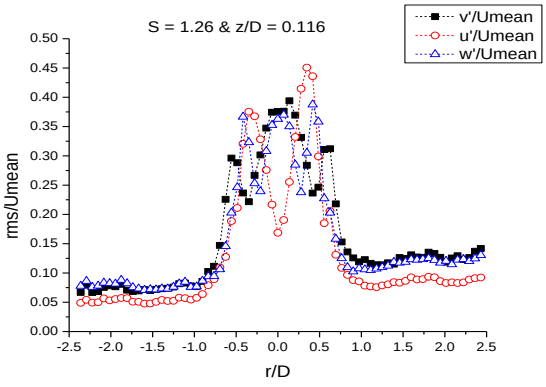

(b)

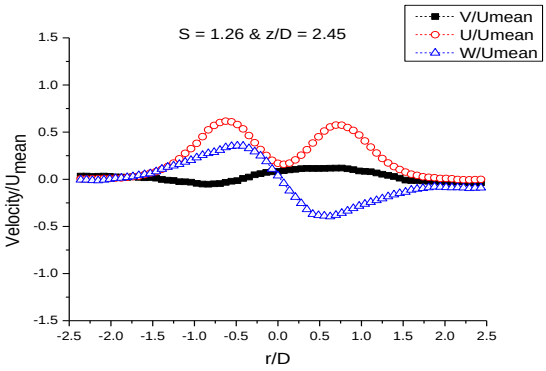

(c)

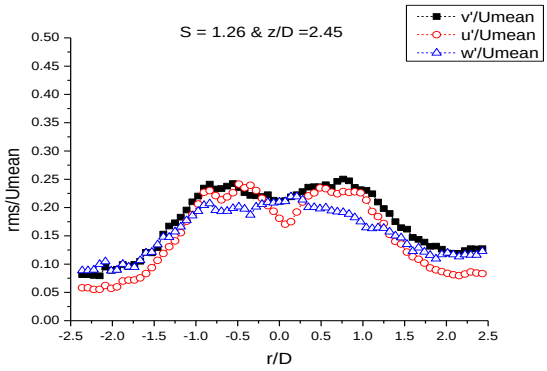

(d)

Fig. 5 (a,c) Mean (left) and **(b,d)** r.m.s (right) velocity profiles for radial (black squares), axial (red dots), tangential (blue traingles) under non-swirling conditions for Re = 21800

5.2 Visualization of the POD modes

The characteristics of the coherent structure in the transverse (TP) and longitudinal (LP) planes were extracted from the PIV snapshots using POD reconstruction of the instantaneous velocity vector fields. The POD analysis was performed for two cases: non-swirling flow (S = 0) and strongly swirling flow (S = 1.26). The total energy fraction and cumulative energy distribution per POD modes for both measurements is shown in Figure 6(a&b). Plot of the individual energy contribution, as a percentage of the total energy, of the POD modes for the non-swirling and the swirling jet is shown in Figure 6a. The energy contribution of first two modes is 18.9 % for TP and 9.3 % for LP for the non-swirling flow and 42.3 % for TP and 12.4 % for LP in case of the swirling jet. For transverse and longitudinal plane, the relative levels of the first mode couple with respect to the total energy are disparate. This is because the predominant structures analyzed by longitudinal measurement are small as compared to transverse domain. For swirling flow case in both planes, the energy fraction of the modes is quite low subsequently after the first two modes and the energy reduction after first two modes is visualized as downward steeper line in Figure 6a. Figure 6b shows the convergence of cumulative energy fraction of the POD modes towards 100 % is relatively faster for swirling flow than for the non-swirling flow for longitudinal plane, and for the transverse plane convergence rate is faster for swirling flow up-to mode 72 $i.e\ \frac{Mode\ Number}{N} \cong 0.103$ approx after that become slower as compared to the non-swirling flow.

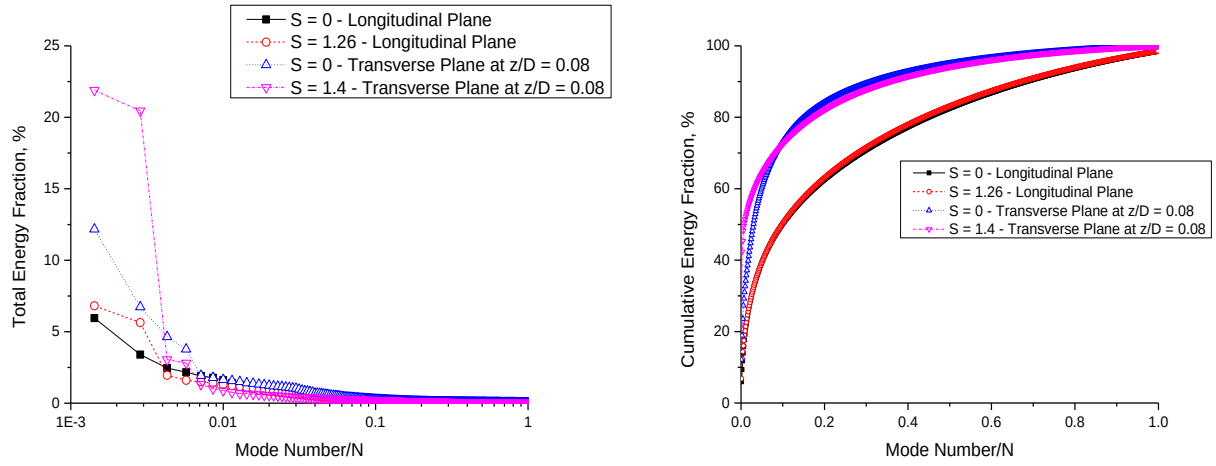

(a) (b)

Fig. 6 (a) Total energy distribution and **(b)** cumulative energy distribution per mode in non-swirling and swirling flow for both transverse (z/ D = 0.08) and longitudinal plane. The mode number is normalized with the number of snapshots (N).

The first and second POD modes for transverse and longitudinal plane are shown in Figure 7(a,b,c&d), only for swirling flow because not such presence of rotating vortices/ coherent structures for non-swirling flow could be evidenced by the POD analysis (POD results for non-swirling case have not been reported here). For transverse plane, Figure 7(a&b), the PVC is represented by varying linear superposition of the first two POD modes. For longitudinal plane, Figure 7(c&d), mode 1 and mode 2 shows the regular organized vortices along the shear layer that represents the coherent structures. Furthermore, the PVC is strongest at the exit of the nozzle and decreasing towards downstream after z/ D =1.5 approximately.

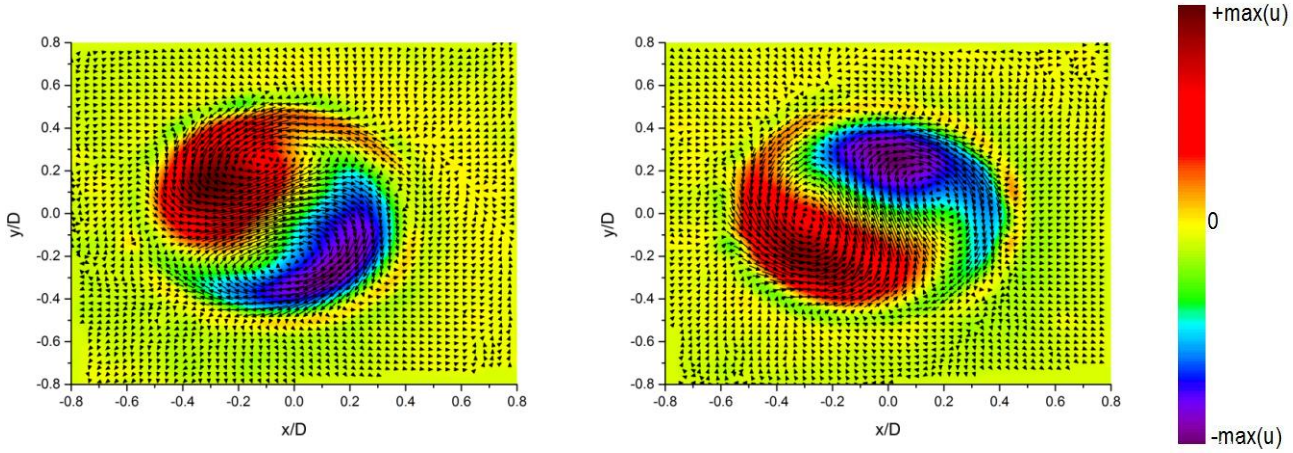

(a) mode 1 (b) mode 2

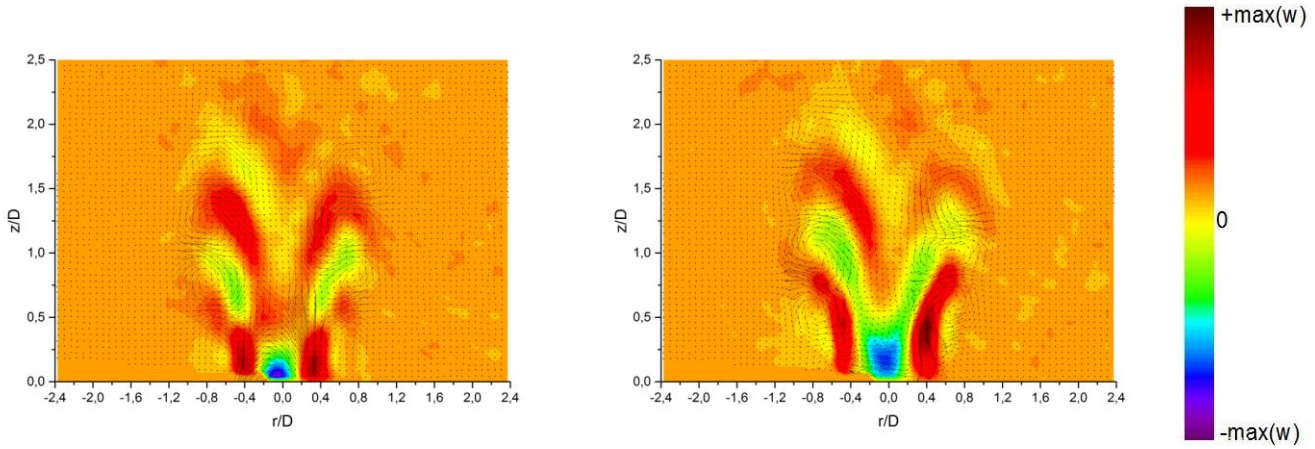

(c) mode 1 (d) mode 2

Fig. 7 Upper row (transverse plane: z/ D = 0.08) and lower row (longitudinal plane): POD mode 1 and mode 2 (vector plot), axial (u) and tangential (w) velocity components (contours).

To illuminate the behavior of the identified coherent structure, the phase portraits of the corresponding amplitudes a_1 and a_2 for both transverse and longitudinal plane are shown in Figure 8(a&c). The phase portrait clearly shows the existence of an oscillating behavior. Oudheusden et al. (2005) and Chong et al. (2013) proposed to calculate the phase angle, φ, for each PIV snapshot with the corresponding time dependent POD mode coefficients a_1 and a_2 as $\varphi = \arctan\left(\frac{a_2}{a_1}\right)$.

Figure 8(b&d) shows a unit circle in the a_1*-a_2* which is obtained by normalizing $a_1^* = a_1/ r_m$ and $a_2^* = a_2/ r_m$. , where $r_m = \sqrt{a_1^2 + a_2^2}$

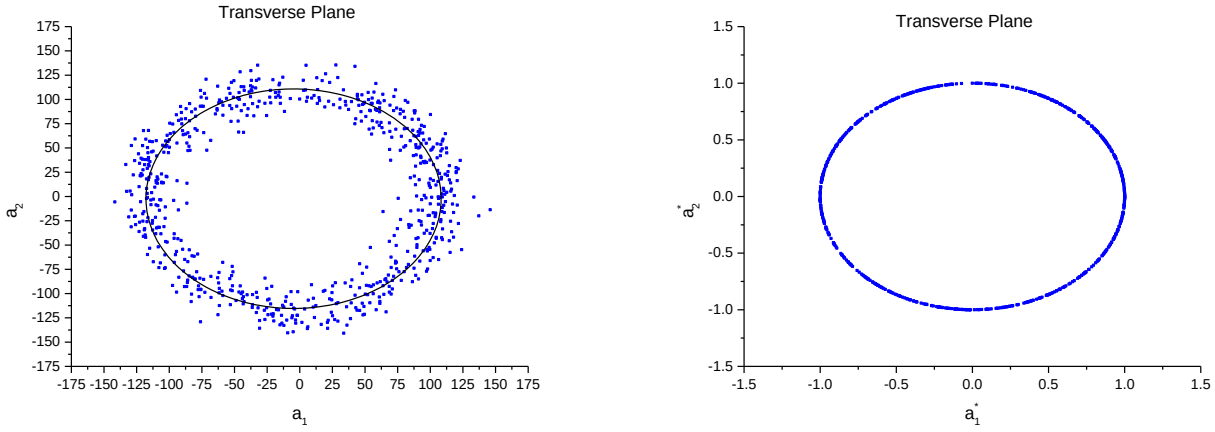

(a) (b)

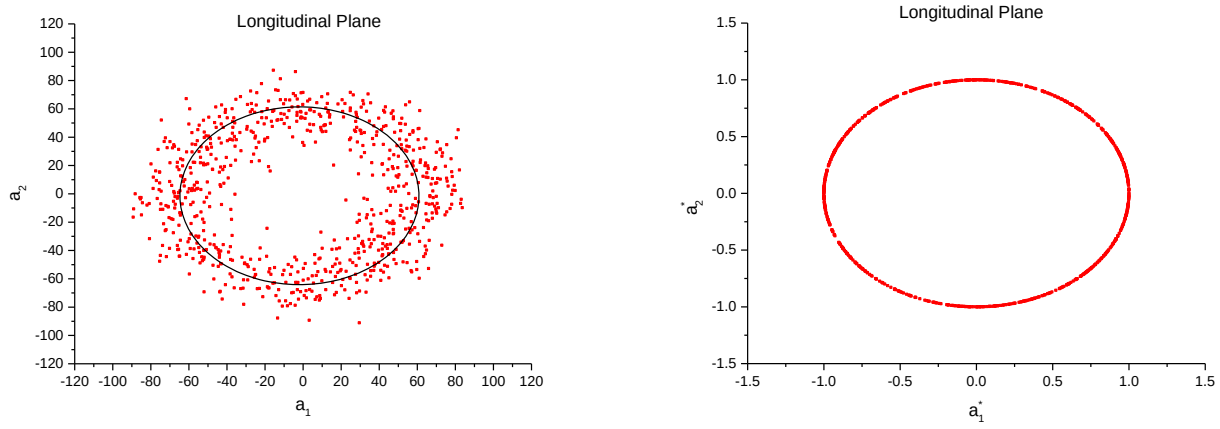

(c) (d)

Fig. 8 Phase portrait of mode coefficients a_1 and a_2 for the transverse (upper row) and longitudinal (lower row) plane. The solid line is a circular fit and similar to Lissajous figure.

The presence of a well defined periodic signal is also characterized by acquiring the pressure fluctuations caused by the flow field by capacitive microphone. A spectral analysis according to the Bartlett method (John et al. 1996) and with a frequency resolution of 1 Hz was applied to the pressure signal to identify the PVC frequency. The environmental temperature and pressure are maintained in the range of 299K and 1bar. The precession of the vortex core is almost periodic and its trademark is clearly visible in the power spectra of pressure oscillation as shown in Figure 9. The PVC is indicated by sharp peak in the spectra at frequency f_{PVC} = 175 Hz, Strouhal number = f_{PVC}*D/ U_{mean}=0.707, where the pulsation amplitude is observed to change rapidly by two orders of magnitude. The presence of a second harmonic is at twice the precession frequency.

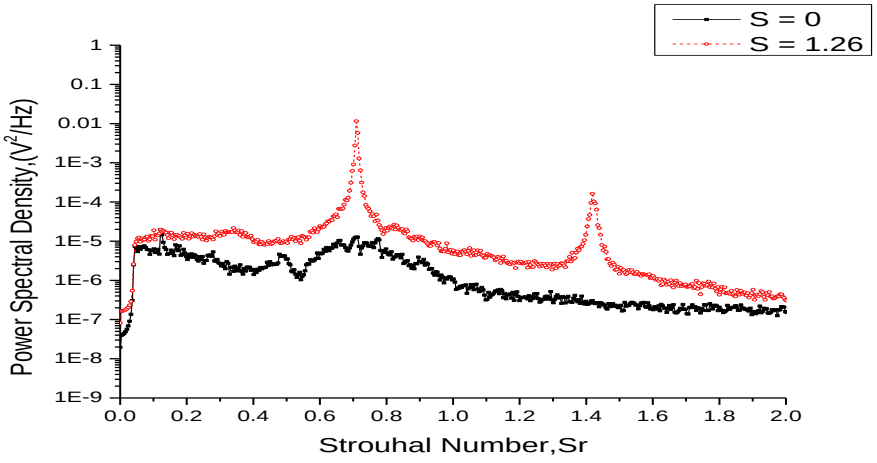

Fig. 9 Power spectral density of the pressure oscillation as a function of frequency. The two peaks at Strouhal number (Sr) = 0.709 and 1.418 evidence the presence of PVC for S = 1.26.

5.3 Conditional phase-averaged of velocity distribution and swirl strength

Figure 10 shows the results of phase averages of velocity field on the longitudinal plane (results with transverse plane are not shown here). On an average 60 instantaneous maps per phase angle for the phase average measurements are available which is quite sufficient for statistical convergence. In particular these figure shows the contours of radial, axial, tangential velocity at φ = 0°, 90°, 180° and 270° normalized with the mean axial velocity at nozzle exit. The phase average velocity contours shows disparity from the time-mean averaged velocity. The shape of oscillation or vortices appear in the shear layer is depicted in every phase of radial velocity contours. Almost non-anti-symmetric structures can be observed for tangential velocity contours and velocity gradients in the shear layer signify the presence of coherent structures above the exit of nozzle. Phase locked axial velocity contours for all phases display asymmetry with respect to the geometrical axis. Recirculation bubble is substantially displaced from the geometric center in the radial direction causing periodic motion at the nozzle exit. Close to the nozzle exit the periodic variation of the axial velocity in the region of $0.2 < \left|\frac{r}{D}\right| < 0.5$ results the high RMS of the axial velocity component while at the nozzle axis, r/ D ≅ 0, due the low axial velocity gradient, fluctuations are much less intense, Figure 5b.

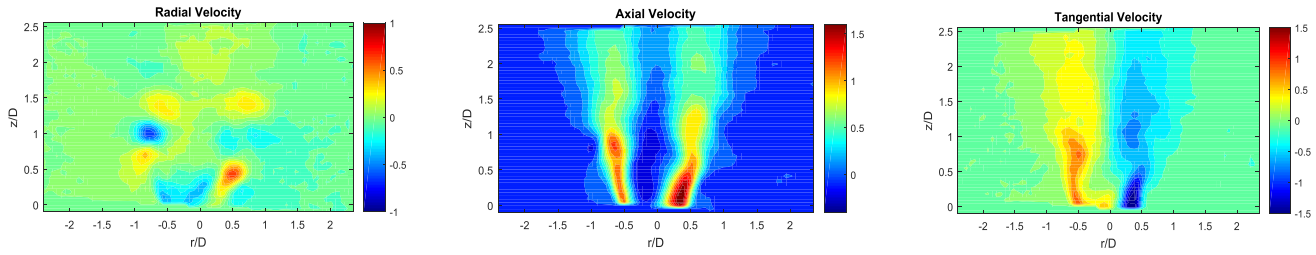

(a) φ = 0

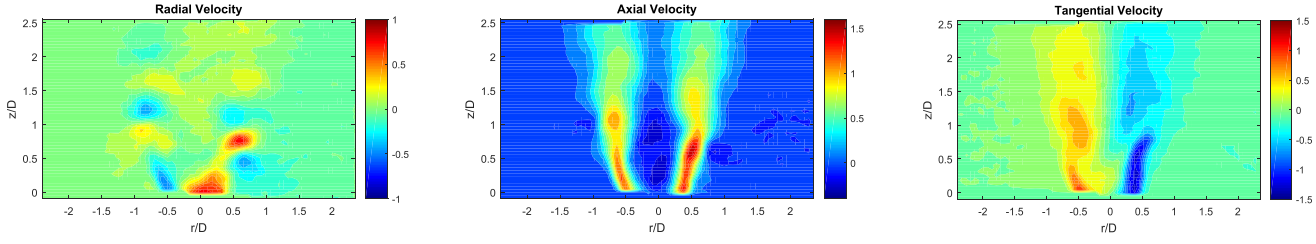

(b) φ = 90°

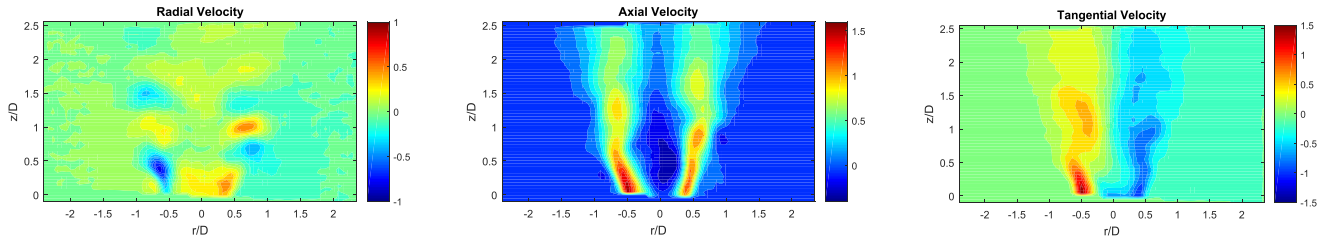

(c) φ = 180°

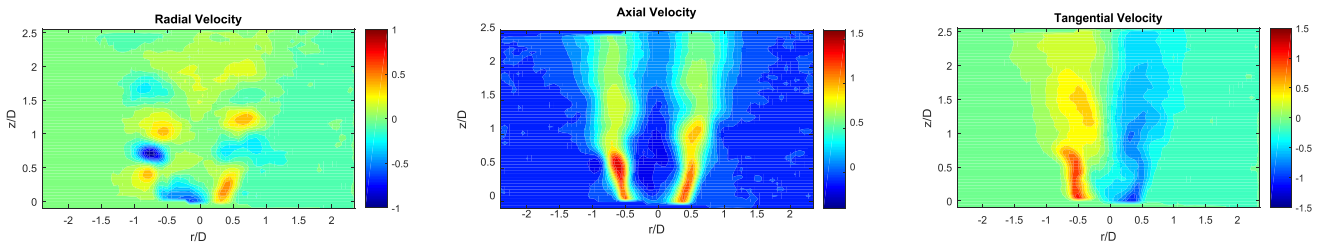

(d) φ =270°

Fig. 10 Phase averages contours of radial (left), axial (middle), tangential (right) velocity at different phases in longitudinal plane.

Analysis of the swirling strength from the instantaneous velocity fields for the unconfined isothermal swirling flow revealed the presence of the spiral vortices at the inner shear layer around the reverse flow region and outer shear layer between the swirling jet and ambient air. Several studies have found that the three dimensional coherent structures rotates around the central axis induced by the PVC (Syred et al. (2006), Cala et al. (2006), Stöhr et al. (2011), Alekseenko et al. (2013)). Figure 11 presents the phase averages of swirling strength with velocity vectors superimposed on it, for the longitudinal plane at φ = 0°, 90°, 180° and 270° respectively. The phase averaged swirling strength shows strong vortices present in the outer shear layer along with weaker vortices in the inner shear layer, this overall structure moves downstream (precess) as the phase angle increases. The two co-winding counter-rotating helical vortices appears to fade out at an axial location of approximately z/ D = 1.5. The 3D helical vortex structure is then reconstructed by using the minima of negative phase averaged swirling strength. Assuming that the phase angle is equal to the angular rotation of the structure and by properly selecting a threshold value, isosurface of the swirling strength can be plot in the 3D space, Figure 12. The two helical vortex structure appears to have different pitch, the vortex in the outer shear layers has a pitch equal to about one nozzle diameter, 2R, while the vortex in the

inner shear layer shows a shorter pitch and equal to about one nozzle radius, R. The presence of a second harmonic in the pressure spectra of Figure 9 could be releated to the difference in helices pitch. The inner helical vortex with half the pitch of the outer one generates pressure oscillation at twice the PVC foundamental frequency (i.e. 175Hz) when convected downstream.

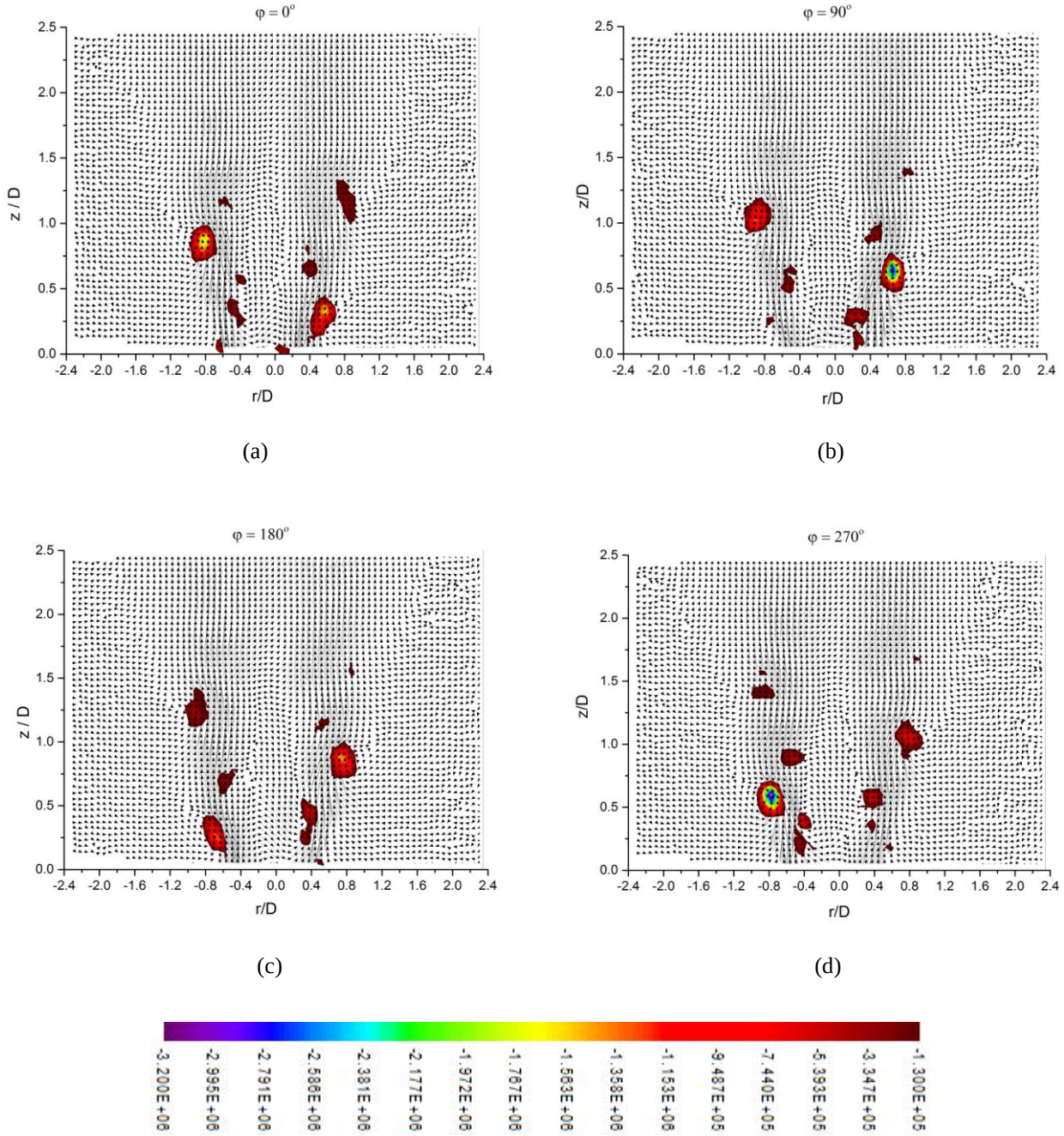

Fig. 11 Phase averages of the swirling strength for φ = 0°, 90°, 180° and 270°. Colors represent the absolute value of swirling strength

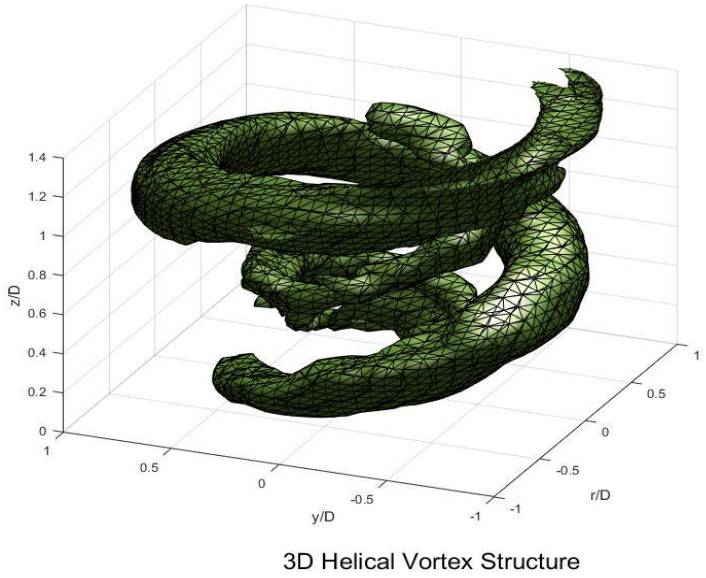

Fig. 12 Iso-surface of swirling strength for the swirling jet, S=1.26

6. Conclusions

The present study reports detailed measurements for both non-swirling and unsteady swirling flow using 3C-2D stereo particle image velocimetry (PIV) and specific acoustic microphone probe. Detailed Stereo-PIV measurements were made for Re = 21800 with two different swirl number (S = 0 and 1.26). The presence of the PVC instability with a frequency of about 175 Hz was indicated by a sharp peak in the spectra of the acoustic pressure fluctuation acquired by a capacitive microphone. The coherent vortex structures of strongly swirling jet undergoing vortex breakdown were also extracted from the measured velocity field by means of POD and phase average technique. The noticeable oscillatory motion of the fluctuations was evidenced by first two most energetic POD modes covering a corresponding vortex structure. The velocity field reconstructed using POD mode showed that the dominant coherent flow structure decreasing towards downstream after z/ D = 1.5 approximately. These two POD modes allowed to determine the phase angle for each instantaneous velocity vector map. Phase angles has been used to phase average the corresponding instantaneous velocity field, the phase averaged velocity maps showed the existence of dominant coherent flow structure. The latter highlighted a much complex flow structure as compared to one observed in the mean flow field. The 3D helical vortex structure has been reconstructed by using threshold value on the minima of negative phase averaged swirling strength and by assuming that the phase angle is equal to the angular rotation of the structure. It reveals two co-winding counter-rotating helical vortices originating in the inner and outer shear layer and this structure fade out at an axial location of

approximately z/ D = 1.5. Moreover, our study demonstrated that the combination of PIV technique with POD tool and specific acoustic microphone probe serves as a powerful approach in the characterization of large scaled organized structures.

Acknowledgements

The authors are pleased to acknowledge the financial support from Politecnico di Milano and Heritage - Erasmus Mundus Action 2 partnership Europe/ India through Research fellowship provided for Rohit Sharma.

Reference

Alekseenko MV, Bilsky AV, Dulin VM, Markovich DM, Tokarev MP (2013) "Tomographic PIV measurements in a swirling jet flow. Proc. 10th International Symposium on Particle Image Velocimetry, 1-3 July 2013, Delft, The Netherlands

Berkooz G, Holmes P, Lumley JL (1993) The proper orthogonal decomposition in the analysis of turbulent flows. Annu Rev Fluid Mech 25:539-575.

Billant P, Chomaz JM, Huerre P (1998) Experimental study of vortex breakdown in swirling jets. J Fluid Mech 376:183–219.

Cala CE, Fernandes EC, Heitor MV, Shtork SI (2006) Coherent structures in unsteady swirling jet flow. Exp Fluids 40:267–276.

Cassidy J, Falvey H (1970) Observations of unsteady flow arising after vortex breakdown. J Fluid Mech 41:727–736.

Chanaud R (1965) Observations of oscillatory motion in certain swirling flows. J Fluid Mech 21:111–127.

Chen H, Reuss DL, Sick V (2012) On the use and interpretation of proper orthogonal decomposition of in-cylinder engine flows. Meas Sci Technol 23: 085302.

Chigier NA, Chervinsky A (1967) Experimental investigation of swirling vortex motion in jets. J Appl Mech 34:443–451.

Chong P, Hongping W, Jinjun W (2013) Phase identification of quasi-periodic flow measured by particle image velocimetry with a low sampling rate. Measurement Science and Technology 24:055305.

Claypole TC, Syred (1981) The Effect of Swirl Burner Aerodynamics on NOx Formation. International Symposium on Combustion 18 (1), 81–89

Cozzi F, Sharma R, Coghe A, Arzuffi F (2015) An experimental investigation on Isothermal free swirling jet. XXXVIII Meeting of the Italian Section of the Combustion Institute, 20-23 September, Lecce, Italy doi: 10.4405/ 38proci2015.I2

Farokhi S, Taghavi R, Rice EJ (1989) Effect of initial swirl distribution on the evolution of a turbulent jet. AIAA J 27(6):700–706.

Gupta AK, Lilley DG, Syred N (1984) Swirl flows. Abacuss Press, London

John G, Proakis Dimitris, Manolakis G (1996) Digital signal processing (3rd ed.): principles, algorithms, and applications, Prentice-Hall, NJ, USA

Liang H, Maxworthy T (2005) An experiment investigation of swirling jets. J Fluid Mech 525:115–159.

Lumley JL (1967) The structure of inhomogeneous turbulence . In: Yaglom AM, Tatarski VI (eds) Atmospheric turbulence and wave propagation. Nauka, Moscow, 166-178.

Martinelli F, Cozzi F, Coghe A (2012) Phase-locked analysis of velocity fluctuations in a turbulent free swirling jet after vortex breakdown. Exp Fluids 53:437-449.

Negri M, Cozzi F, Malavasi S (2010) Self-synchronized phase averaging of PIV measurements in the base region of a rectangular cylinder. Meccanica 46: 423-435.

Oberleithner K, Sieber M, Nayeri CN, Paschereit CO, Petz C, Hege HC (2011) Three-dimensional coherent structures in a swirling jet undergoing vortex breakdown: stability analysis and empirical mode construction. J Fluid Mech 679:383-414.

Panda J, McLaughlin DK (1994) Experiments on the instabilities of a swirling jet. Phys Fluids 6(1):263–276.

Rajaratnam N (1976) Turbulent Jets. Elsevier, Amsterdam

Sirovich L (1987) Turbulence and the dynamics of coherent structures. Quart Appl Math 45: 561-590.

Soloff SM, Adrian RJ, Liu ZC (1997) Distortion compensation for generalized stereoscopic particle image velocimetry. Meas. Sci. Technol.8:1441-1454.

Stohr M, Sadanandan R, Meier W (2011) Phase-resolved characterization of vortex-flame interaction in a turbulent swirl flame. Exp Fluids 51:1153-1167.

Syred N (2006) A review of oscillation mechanisms and the role of the precessing vortex core (PVC) in swirl combustion systems. Prog Energy Comb Sci 32:93–161.

van Oudheusden BW, Scarano F, van Hinsberg NP, Watt DW (2005) Phase-resolved characterization of vortex shedding in the near wake of a square-section cylinder at incidence. Exp Fluids 39: 86-98.